Originally published as:

Darugna F., Steigenberger P., Montenbruck O, Casotto S. (2018): Ray-Tracing Solar Radiation Pressure Modeling for QZS-1, Advances in Space Research, Vol. 62, No. 4, pp. 935 – 943, DOI: 10.1016/j.asr.2018.05.036

The original publication is available at http://www.elsevier.com

Ray-Tracing Solar Radiation Pressure Modeling for QZS-1

Francesco Darugna[a,b], Peter Steigenberger[c], Oliver Montenbruck[c] and Stefano Casotto[d]

[a]Università degli Studi di Padova, Department of Industrial Engineering, Via Gradenigo 6/a, 35131 Padova, Italy
[b]Geo++ GmbH, Steinriede 8, 30827 Garbsen, Germany
[c]Deutsches Zentrum für Luft- und Raumfahrt (DLR), German Space Operations Center (GSOC), Münchener Straße 20, 82234 Weßling, Germany
[d]Università degli Studi di Padova, Department of Physics and Astronomy, Vicolo dell'Osservatorio 3, 35122 Padova, Italy

Abstract Precise orbit determination requires accurate models for the orbital perturbations. Next to the well-known gravitational forces, the solar radiation pressure (SRP) is the main perturbation for navigation satellites. SRP results from the interaction between the photons of the Sun and the surfaces of the satellite. Hence, its modeling depends on proper knowledge of the geometry and optical properties of the satellite. Previous work showed that the use of an a priori box-wing model for the SRP significantly improves the estimated orbit products as well as orbit predictions compared to purely empirical models. However, the presently available box-wing models for the first satellite of the Japanese Quasi-Zenith Satellite System, QZS-1, do not consider an accurate geometry. Based on a computer-aided design model of the QZS-1 satellite, a ray-tracing simulation is performed to compute SRP accelerations in a more realistic manner. The resulting SRP model is validated through QZS-1 precise orbit determination over a two year data arc covering yaw-steering and orbit-normal attitude regimes. In yaw-steering mode, the ray-tracing model shows a better overall performance than a box-wing model and improves the standard deviation of QZS-1 satellite laser ranging residuals by a factor of three compared to orbits without a priori model. On the other hand, the ray-tracing SRP model does not account for thermal accelerations and thus performs worse than an adjusted box-wing model in orbit-normal mode.

Keywords: Solar radiation pressure, ray-tracing model, QZSS, SLR

1 Introduction

Solar radiation pressure (SRP) is the dominant non-gravitational perturbation for global (and regional) navigation satellite systems (GNSSs) that require cm-level orbit knowledge for high-precision geodetic applications (Bock and Melgar, 2016). Therefore, precise orbit determination (POD) of GNSS satellites requires an accurate SRP model. Since Earth gravity field and luni-solar gravitational perturbations are well described nowadays, the SRP represents the key objective for precise orbit determination and prediction of the satellites mentioned above. So far, different kinds of SRP models have been developed: models based on ray-tracing and thermal analysis (Ziebart, 2004; Gini, 2014), analytical and semi-analytical models based on generic box-wing models (Rodriguez-Solano et al., 2012) and purely empirical models such as the empirical CODE orbit model (ECOM; Beutler et al., 1994; Springer et al., 1999) and its successor ECOM-2 (Arnold et al., 2015), developed at the Center for Orbit Determination in Europe (CODE).

Models based on ray-tracing techniques require an accurate description of the geometrical and optical properties of the satellite, while box-wing models only consider a simplified spacecraft geometry. ECOM and ECOM-2 do not require a priori information, but their performance depends on the selection of the estimated parameters. These parameters are given in a Sun-oriented DYB-frame with D pointing towards the Sun, Y along the solar panels axis, and B completing a right-handed system. For ECOM, usually five parameters are estimated: three constant terms in D-, Y-, B-direction and sine/cosine terms in B-direction. ECOM-2 adds higher harmonic terms but usually only the 2nd and 4th order terms in D-direction are considered resulting in a total number of nine parameters. It is important to select an appropriate set of ECOM parameters in order to take into account the properties of the spacecraft and to ensure that all parameters are observable. As an example, the 5-parameter ECOM resulted in large systematic errors for the Galileo satellites (Steigenberger et al., 2015a) that could be overcome by estimating the additional parameters of ECOM-2 (Prange et al., 2017).

The deployment of the Quasi-Zenith Satellite System (QZSS; Inaba et al., 2009; Kogure et al., 2017), the Japanese regional navigation satellite system, started in 2010 with its first satellite QZS-1 ("Michibiki"). QZSS broadcasts GPS-compatible signals to serve as an augmentation system for GPS and to provide highly precise and stable positioning services, focusing on the Asian-Pacific region. The orbit of QZS-1 is an elliptical inclined geosynchronous orbit (IGSO) in order to spend a longer time over the Japanese region than over the other regions. Between June and October 2017, two 2nd generation IGSO satellites (QZS-2 and -4) as well as a geostationary satellite (QZS-3) were launched (Cabinet Office, 2017a). The QZSS service will start in 2018 and offer three simultaneously visible satellites at all times from locations in the Asia-Oceania regions (Cabinet Office, 2017a). Expansion into a seven-spacecraft constellation using both IGSO and geostationary orbits is expected by 2023 (Kogure, 2016).

QZS-1 employs two different attitude modes: the yaw-steering (YS) mode and the orbit-normal (ON) mode (Ishijima et al., 2009), depending on the elevation of the Sun above the or-

bital plane (β-angle). In nominal YS mode, which is employed for $|\beta| > 20°$, the solar panel axis is perpendicular to the Sun and Earth directions and the navigation antenna points towards the Earth (Bar-Sever, 1996). For $|\beta| < 20°$, the spacecraft switches to ON attitude, in which the solar panel axis is maintained perpendicular to the orbital plane (Montenbruck et al., 2015).

Similar to Galileo, QZS-1 has an elongated body shape that has to be taken into account in the SRP modeling. The two different attitude modes have been considered in the development of a semi-analytical box-wing model by Montenbruck et al. (2017a). This model combines an analytic a priori model with a set of five empirical ECOM parameters and achieves a significant improvement w.r.t. the use of purely empirical models. QZS-1 orbits obtained in this way show a better than 10 cm RMS consistency with satellite laser ranging (SLR) measurements, the day boundary discontinuities are reduced by two thirds w.r.t. the orbits obtained without any a priori model and the orbit-clock variations are reduced by up to 85% during ON mode. Nevertheless, the use of a box-wing model cannot completely remove orbit errors and the necessity of estimating empirical SRP parameters. The performance of a box-wing model as a priori model in POD for QZS-1 has been also investigated in Zhao et al. (2018). The results of that work show also that the combination of ECOM with an a priori box-wing model can improve the quality of the estimated orbits by up to a factor of three compared to orbits without a priori model, and achieves RMS SLR residuals of 8 cm in YS mode. However, Montenbruck et al. (2017a) and Zhao et al. (2018) had to make assumptions about geometry and optical properties of QZS-1 as no detailed information about these was available at the time of those studies.

Ray-tracing techniques consider a computer-aided design (CAD) model which allows to take into account the geometric properties of the satellite and its individual components in great detail. For instance, ray-tracing techniques have been used for the precise orbit determination of GLONASS (Ziebart, 2004) and the low Earth orbit gravity field mission GOCE (Gini, 2014), improving the estimated orbits of these spacecraft. In Gini (2014) the ray-tracing model for the SRP reduced the empirical acceleration by about 20 %. Within the present study all ray-tracing computations were performed with the commercial Zemax OpticStudio software, which has earlier been suggested for SRP modeling by Gini (2014).

This paper extends the work described in Montenbruck et al. (2017a) and aims to achieve a better SRP description by taking into account the detailed structure of QZS-1. Therefore, a ray-tracing model of solar radiation pressure for the QZS-1 satellite described by a CAD geometry is developed. The reference frames involved in this work, i.e., the YS, the ON, and the body-fixed frame, are introduced in Sect. 2. The geometrical and optical properties are described in Sect. 3 taking into account the previous considerations about QZS-1. The ray-tracing approach is described in Sect. 4 together with the implementation of the model into an optics software. The results of the ray-tracing are then used to compute gridded accelerations, which can be easily introduced into the POD software. The performance of the QZS-1 ray-tracing model in precise orbit determination is evaluated in Sect. 5 by analyzing estimated ECOM parameters, SLR residuals, day boundary discontinuities, and orbit predictions. We furnish also a critical comparison with the results obtained with the semi-analytical model presented in Montenbruck et al. (2017a) and the empirical ECOM-2 model (Arnold et al., 2015).

2 Reference frames

Unlike the 2nd generation QZSS IGSO satellites, QZS-1 employs two different attitude modes: the YS mode and the ON mode (Cabinet Office, 2017b). Within the YS mode, the x,y,z spacecraft body axis as defined by the manufacturer are nominally aligned with a YS frame defined in the following way:

$$\begin{aligned} \boldsymbol{e}_{x,\mathrm{YS}} &= \boldsymbol{e}_{y,\mathrm{YS}} \times \boldsymbol{e}_{z,\mathrm{YS}} \\ \boldsymbol{e}_{y,\mathrm{YS}} &= -\frac{\boldsymbol{e}_{\odot} \times \boldsymbol{r}}{|\boldsymbol{e}_{\odot} \times \boldsymbol{r}|} \\ \boldsymbol{e}_{z,\mathrm{YS}} &= -\frac{\boldsymbol{r}}{|\boldsymbol{r}|} \,. \end{aligned} \tag{1}$$

Here, $\boldsymbol{e}_{\odot}$ is the unit vector pointing from the satellite towards the Sun and $\boldsymbol{r}$ is the satellite position relative to the center of the Earth. Vice versa, the body axis in ON mode are aligned with the unit vectors

$$\begin{aligned} \boldsymbol{e}_{x,\mathrm{ON}} &= \boldsymbol{e}_{y,\mathrm{ON}} \times \boldsymbol{e}_{z,\mathrm{ON}} \\ \boldsymbol{e}_{y,\mathrm{ON}} &= -\frac{\boldsymbol{r} \times \boldsymbol{v}}{|\boldsymbol{r} \times \boldsymbol{v}|} \\ \boldsymbol{e}_{z,\mathrm{ON}} &= -\frac{\boldsymbol{r}}{|\boldsymbol{r}|} \,, \end{aligned} \tag{2}$$

where $\boldsymbol{v}$ denotes the inertial velocity vector of the satellite.

3 Geometrical and optical properties of QZS-1

The launch of QZS-1 in September 2010 initiated the build-up of the four-satellite QZSS constellation, which was ultimately completed in late 2017. The inclined geosynchronous orbit of QZS-1 has a $23^{\mathrm{h}}56^{\mathrm{m}}$ orbital period, an inclination of about 43° and a slight eccentricity of $e = 0.075$ to maximize the visibility over Japan (Kogure et al., 2017). Compared to GPS or Galileo, QZS-1 is a big satellite with an envelope of about 3 m × 3 m × 6 m and a span width of 25 m (Inaba et al., 2009; JAXA, 2010). However, there is only limited published information concerning the size and optical properties of the different spacecraft components. In October 2017, satellite property information and operational history information were published by the Cabinet Office, Government of Japan (CAO; Cabinet Office, 2017b, 2018). However, the geometrical information is essentially limited to the dimensions of encompassing boxes of the body and panels, and no optical properties of individual surface materials have yet been made available.

Therefore, more detailed geometrical properties of QZS-1 were obtained from a paper model originally made available by the Japanese Aerospace Exploration Agency (JAXA)[1]. Based on this scaled model, a CAD description of the satellite has been

[1]The original website is no longer available, but a copy is retained at https://web.archive.org/web/20170624175520/qz-vision.jaxa.jp/READ/qz-craft.html

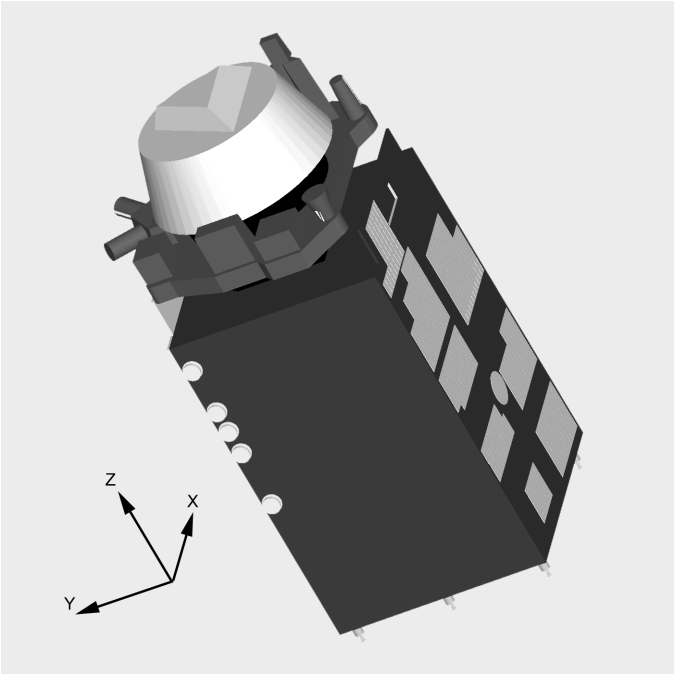

Figure 1: CAD representation of the QZS-1 body as used for the ray-tracing simulation.

generated. The resulting model for the main satellite body is shown in Fig. 1. The Earth-facing side carries a support structure hosting the large L-band GNSS antenna and other components such as the C-band telemetry, command antennas, retro-reflector array and star trackers. The overall dimensions of the satellite obtained from the paper model agree with the values published in Cabinet Office (2017b) within 5 cm.

For a general SRP model, both the incidence direction of the Sun light and the rotation angle of the solar panels relative to the spacecraft body need to be considered. However, notable simplifications can be made in this process by independently considering the body and panel contributions to the SRP. This is possible for QZS-1, since the main panels do not cast a shadow on the body and vice versa in both attitude modes. To facilitate computations, the ray-tracing simulations have therefore been confined to the satellite body only, whereas the SRP contribution of the solar panels can directly be described by analytical expressions for the YS and ON attitude modes (Montenbruck et al., 2017a) and does not require a more detailed ray-tracing.

Since there are presently no published values of the optical properties of QZS-1, they are assumed based on the different kinds of materials used for the spacecraft:

- multi-layer insulation (MLI) with an outer carbon-filled layer to prevent electrostatic charging;
- the radome made from a different type of radiofrequency transparent silver MLI;
- mirror-like optical solar reflectors (OSRs) acting as thermal radiators.

The values of the optical properties assumed for these different surfaces are the same as presented in Montenbruck et al. (2017a) and are summarized in Table 1.

The black MLI is a highly absorptive material, whereas the OSR consists of an almost perfect specularly reflecting material. The silver MLI, in contrast, has a balanced absorptivity and diffuse reflectivity at a very low specular reflectivity. Optical properties for the solar panels will be discussed in Sect. 5 along with the impact of Earth radiation pressure on the overall satellite.

Table 1: Optical properties of the different materials of the QZS-1 spacecraft body as assumed in Montenbruck et al. (2017a).

Material	α	δ	ρ
Black multi-layer insulation	0.94	0.06	0.00
Silver multi-layer insulation	0.44	0.46	0.10
Optical solar reflector	0.06	0.00	0.94

4 Ray-tracing Solar Radiation Pressure Model

The ray-tracing approach simulates the interaction between a beam of photons coming from the Sun and the diverse surface elements of the spacecraft. Detailed knowledge of the geometrical and optical properties of the satellite is a prerequisite for this technique. Within the present study, the illuminated surfaces are first identified and the corresponding incidence angles are computed with the Zemax OpticStudio ray-tracing software. This information is subsequently used to derive accelerations with the ARPA (Aerodynamics and Radiation Pressure Analysis) software package.

4.1 Ray-tracing with OpticStudio

Zemax OpticStudio is a commercial ray-tracing software with primary applications in the design of optical systems. Based on a CAD description of the geometry of an object and the definition of a light source, the propagation of individual rays can be simulated. For SRP simulations, the solar illumination is considered as a parallel beam of light with rectangular cross-section, whose sides are longer than the longest dimension of the body of interest and a central ray that passes through the center of the spacecraft coordinate system. The incidence direction of the individual rays is described by the azimuth angle α and the elevation ε as illustrated in Fig. 2.

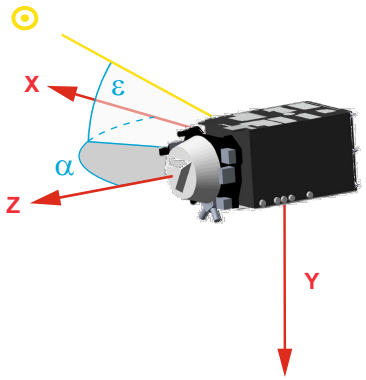

Figure 2: Illustration of azimuth α and elevation ε of the Sun ($\odot$) in the manufacturer-defined spacecraft body frame.

Within the YS mode, the Sun is always confined to the x/z-plane ($\varepsilon = 0$) with $180^\circ \leq \alpha \leq 360^\circ$. In ON mode in contrast, the elevation may attain values of up to $\pm 20^\circ$ and α covers a full circle within one revolution. Accordingly, all ray-tracing computations have been performed over a grid of azimuth values $\alpha \in [0^\circ, 360^\circ]$ and elevations $\varepsilon \in [-20^\circ, +20^\circ]$ with a step size of 1° in each axis.

For a given Sun incidence angle, a pre-defined number of individual rays are simulated, which start from the source and impinge the surfaces of the spacecraft. In our application, the light source is modeled as a square grid of pixels with a resolution of $0.1\,\mathrm{m}$ in each dimension. This resolution has been adopted in consideration of the smallest structures covered by our simplified CAD model and the available computational resources. Following Li et al. (2018), this grid resolution may induce uncertainties at the $1\,\%$ level into the overall SRP. However, a higher resolution did not appear justified for our work in view of the limited knowledge of the spacecraft geometry and optical properties. The simulation in OpticStudio considers also multiple reflections when a ray, which has impinged first a surface, subsequently impacts other surfaces of the satellite. The considered number of multiple reflections is set to three covering more than $99\,\%$ of the total intersections (Li et al., 2018).

The ray-tracer identifies all surfaces impinged by the rays for a particular illumination geometry. For each of these rays, the output of OpticStudio is given by

- the identification number of each surface element impinged by the ray (potentially including multiple reflections),
- the corresponding incidence direction(s), and
- the surface normal vector(s).

These quantities are subsequently used along with optical properties of the respective surface elements to compute the total SRP accelerations acting on the spacecraft.

4.2 Single-Surface Solar Radiation Pressure Modeling

Following Milani et al. (1987), the acceleration $\boldsymbol{a}_{\mathrm{SRP}}$ contributed by an individual surface element of area A is given by

$$\boldsymbol{a}_{\mathrm{SRP}} = -\frac{\Phi}{mc} A \cos\theta \cdot \left[(\alpha + \delta)\boldsymbol{e}_\odot + \frac{2}{3}\delta \boldsymbol{e}_n + 2\rho \cos\theta \boldsymbol{e}_n \right], \tag{3}$$

where $\boldsymbol{e}_\odot$ denotes the unit vector in Sun direction, $\boldsymbol{e}_n$ is the unit vector perpendicular to the surface element, and θ the angle between both vectors. Furthermore, m denotes the total mass of the satellite, c is the vacuum velocity of light, and $\Phi \approx 1367\,\mathrm{W/m^2}$ denotes the solar irradiance at the mean Sun-Earth distance. The coefficients α, δ and ρ describe the fractions of absorbed, diffusely and specularly reflected radiation.

For surfaces covered by MLI, an almost instantaneous reradiation of the absorbed sunlight has to be considered (Cerri et al., 2010; Adhya, 2005; Rodriguez-Solano et al., 2012). Assuming diffuse reradiation, the additional acceleration amounts to

$$\boldsymbol{a}_{\mathrm{RR}} = -\frac{\Phi}{mc} \cdot A \cos\theta \cdot \frac{2}{3}\alpha \cdot \boldsymbol{e}_n\,. \tag{4}$$

When adding this contribution to Eq. (3), the total acceleration

$$\boldsymbol{a}_{\mathrm{SRP}} = -\frac{\Phi}{mc} A \cos\theta \cdot \left[(\alpha + \delta)(\boldsymbol{e}_\odot + \frac{2}{3}\boldsymbol{e}_n) + 2\rho \cos\theta \boldsymbol{e}_n \right] \tag{5}$$

is obtained for the respective surface element.

4.3 Computation of accelerations with ARPA

The information obtained from the ray-tracing provides the input for the computation of accelerations based on Eqns. (3) and (5). These are performed with the Aerodynamics and Radiation Pressure Analysis (ARPA; Gini, 2014) package developed at the University of Padua. ARPA allows to compute non-gravitational forces and torques acting on a satellite due to solar radiation pressure, Earth radiation pressure, satellite thermal reradiation, and atmospheric drag. For the purpose of this work it is only used to compute the SRP acceleration, since the thermal properties are not publicly available and atmospheric drag is negligible for GNSS satellites.

ARPA associates the individual surface elements as used in the ray tracing software with the optical properties as given in Table 1. Using the geometry of incident rays and surface normal vectors, the contribution of each simulated ray is evaluated and the sum over all rays gives the total force for a particular illumination geometry. At an incidence angle θ, the cross section $A_{\mathrm{pixel}} = 1\,\mathrm{dm^2}$ of the associated beam of light and the illuminated surface area A are related by

$$A_{\mathrm{pixel}} = A \cdot \cos\theta\,. \tag{6}$$

For a single reflection, the force

$$\boldsymbol{F} = -F_{\mathrm{pixel}} \cdot \boldsymbol{f}_{\mathrm{op}} \tag{7}$$

associated with the individual ray can thus be partitioned into the product of a scale factor

$$F_{\mathrm{pixel}} = \frac{\Phi A_{\mathrm{pixel}}}{c} \tag{8}$$

that describes the net force exerted on a fully absorptive body and a dimensionless vector $\boldsymbol{f}_{\mathrm{op}}$ that aggregates the optical properties and the ray/surface-geometry. Depending on the consideration of reemission, it is given by either

$$\boldsymbol{f}_{\mathrm{op}} = (\alpha + \delta)\boldsymbol{e}_\odot + \frac{2}{3}\delta \boldsymbol{e}_n + 2\rho \cos\theta \boldsymbol{e}_n \tag{9}$$

for surfaces not covered by MLI (e.g., optical solar reflector and solar panels) or

$$\boldsymbol{f}_{\mathrm{op}} = (\alpha + \delta)(\boldsymbol{e}_\odot + \frac{2}{3}\boldsymbol{e}_n) + 2\rho \cos\theta \boldsymbol{e}_n \tag{10}$$

for MLI in analogy with Eqns. (3) and (5).

When considering multiple reflections it is assumed that the effects of the second and further reflections due to the diffusive component are small w.r.t. the specularly reflected component, and can thus be neglected (Gini, 2014). As a result, multiple reflections can be taken into account by summing the individual contributions

$$\boldsymbol{F} = -\sum_{j=1}^{n} F_{\mathrm{pixel}}^{(j)} \cdot \boldsymbol{f}_{\mathrm{op}}^{(j)} \tag{11}$$

Table 2: Reduced box-wing model of QZS-1 for Earth radiation pressure modeling.

Surface	Spectral range	Area [m^2]	α	ρ	δ	Reference
$+z$	visible	6	0.60	0.33	0.07	Montenbruck et al. (2017a)
	infrared		0.8	0.1	0.1	Rodriguez Solano (2009)
solar panel front	visible	40	0.75	0.04	0.21	Montenbruck et al. (2017a)
	infrared		0.8	0.1	0.1	Rodriguez Solano (2009)
solar panel back	visible	40	0.89	0.055	0.055	Rodriguez Solano (2009)
	infrared		0.8	0.1	0.1	Rodriguez Solano (2009)

where n denotes the total number of surface hits, while

$$F^{(1)}_{\text{pixel}} = \frac{\Phi A_{\text{pixel}}}{c} \tag{12}$$

and

$$F^{(j)}_{\text{pixel}} = F^{(j-1)}_{\text{pixel}} \cdot \rho_{j-1} = \frac{\Phi A_{\text{pixel}}}{c} \prod_{k=1}^{j-1} \rho_k \tag{13}$$

for $j > 1$ provide the normalized force associated with the beam upon the j-th incidence of the ray on a surface.

The final output of ARPA comprises grids of the total force $\boldsymbol{F}$ for each pair of angles (α, ε) in the predefined azimuth and elevation grid. These values are then divided by the spacecraft mass to obtain the SRP acceleration for the orbit modeling. Based on Cabinet Office (2018) a mass of $m = 2260\,\text{kg}$ has been adopted for the period covered in this study. Accelerations at arbitrary angles α and ε are obtained through bi-linear interpolation from the precomputed grid values.

5 Model Validation

GPS and QZSS observations of a network of 130 stations have been processed with the NAPEOS v3.3.1 software package (Agueda and Zandbergen, 2004) for a two-year period from January 2015 to December 2016. Most stations are multi-GNSS stations provided by the Multi-GNSS Pilot Project (MGEX, Montenbruck et al., 2017b) of the IGS (Dow et al., 2009; IGS, 2017). Depending on the time within the study period, 30 – 55 stations offer QZS-1 tracking capability. In addition, legacy IGS stations have been considered in order to densify the tracking network in areas with sparse GPS tracking coverage. The ionosphere-free linear combination of L1 and L2 observations is used for both, GPS and QZSS. The estimation parameters for each 3-day orbital arc include station coordinates, troposphere zenith delays, Earth rotation parameters, receiver and transmitter clock offsets, inter-system biases, as well as orbital parameters. Ambiguities are only fixed for GPS with the Melbourne-Wübbena approach (Melbourne, 1985; Wübbena, 1985). More details on the GNSS data processing are given in Table 2 of Montenbruck et al. (2017a). In the current work, the IGS14 reference frame (Rebischung et al., 2016a) and the igs14.atx antenna model (Rebischung et al., 2016b) are used. Antenna thrust (Steigenberger et al., 2018) is considered with a transmit power of 250 W (Cabinet Office, 2017b). Accelerations due to Earth albedo and infrared radiation (Knocke, 1989) are considered with a simplified box-wing model and monthly radiation maps. Only the $+z$-surface of the box as well as the front and back side of the solar panels are modeled, since only these surfaces can be oriented towards the Earth in the nominal YS and ON attitude modes. Surface areas and optical properties in the visual and infrared regime as adopted for Earth radiation pressure modeling in this study are listed in Table 2.

Four solutions with different orbit modeling options for QZS-1 have been computed:

- 5-parameter ECOM (without a priori model),
- 9-parameter ECOM-2 (without a priori model),
- a priori box-wing model plus 5-parameter ECOM,
- a priori ray-tracing model plus 5-parameter ECOM.

Since ECOM and ECOM-2 are neither intended nor well-suited for stand-alone use in ON mode (Prange et al., 2017; Montenbruck et al., 2017a), these models are only considered in the YS mode. For the other solutions, a modified $\overline{\text{DYB}}$-frame (Montenbruck et al., 2017a) is used in ECOM during ON mode. Here, $\overline{\text{D}}$ is the projection of the Sun direction on the orbital plane, which is spanned by the $\overline{\text{Y}}$ and $\overline{\text{B}}$ vectors. As discussed in Montenbruck et al. (2017a), this frame is more suitable to describe the SRP accelerations in ON mode than the original DYB-frame.

Figure 3 shows the estimated ECOM parameters for the solutions without a priori model and with a priori box-wing or ray-tracing model. The β-dependency of the estimated D_0 parameter in YS mode is significantly reduced by applying the a priori model. In ON mode, the box-wing model has no β-dependency, whereas the ray-tracing model shows D_0 variations of about $3.5\,\text{nm/s}^2$. The situation is similar for Y_0: in YS mode, box-wing and ray-tracing model provide almost constant estimates close to zero, whereas larger variations of $4\,\text{nm/s}^2$ are present for the ray-tracing model in ON mode. For B_0 systematic effects with an amplitude of about $1\,\text{nm/s}^2$ in YS mode are present for all three solutions but the absolute value is slightly smaller (by $1\,\text{nm/s}^2$) for the solutions with a priori model. The systematic effects for the cosine and sine parameters B^*_C and B^*_S in YS mode are considerably reduced by applying an a priori model. In ON mode, the B^*_C estimates of the ray-tracing model have an offset of about $-1.5\,\text{nm/s}^2$ whereas the box-wing model has no such bias. For B^*_S the opposite situation is encountered: while the ray-tracing model shows no offset between YS and ON mode, the box-wing model shows a mean offset of about $1\,\text{nm/s}^2$ and a slope of $1.5\,\text{nm/s}^2$ during ON mode.

In general, one would expect a decrease in the magnitude of the estimated empirical parameters when using an improved a priori SRP model, as well as a reduction of systematic patterns in these parameters. During YS mode, both the box-wing and the ray-tracing a priori model yield a notable and roughly similar reduction in the empirical parameters. However, during ON mode the ray-tracing model shows systematic effects in the order of a few nm/s^2 for D_0 and Y_0 due to unmodeled thermal

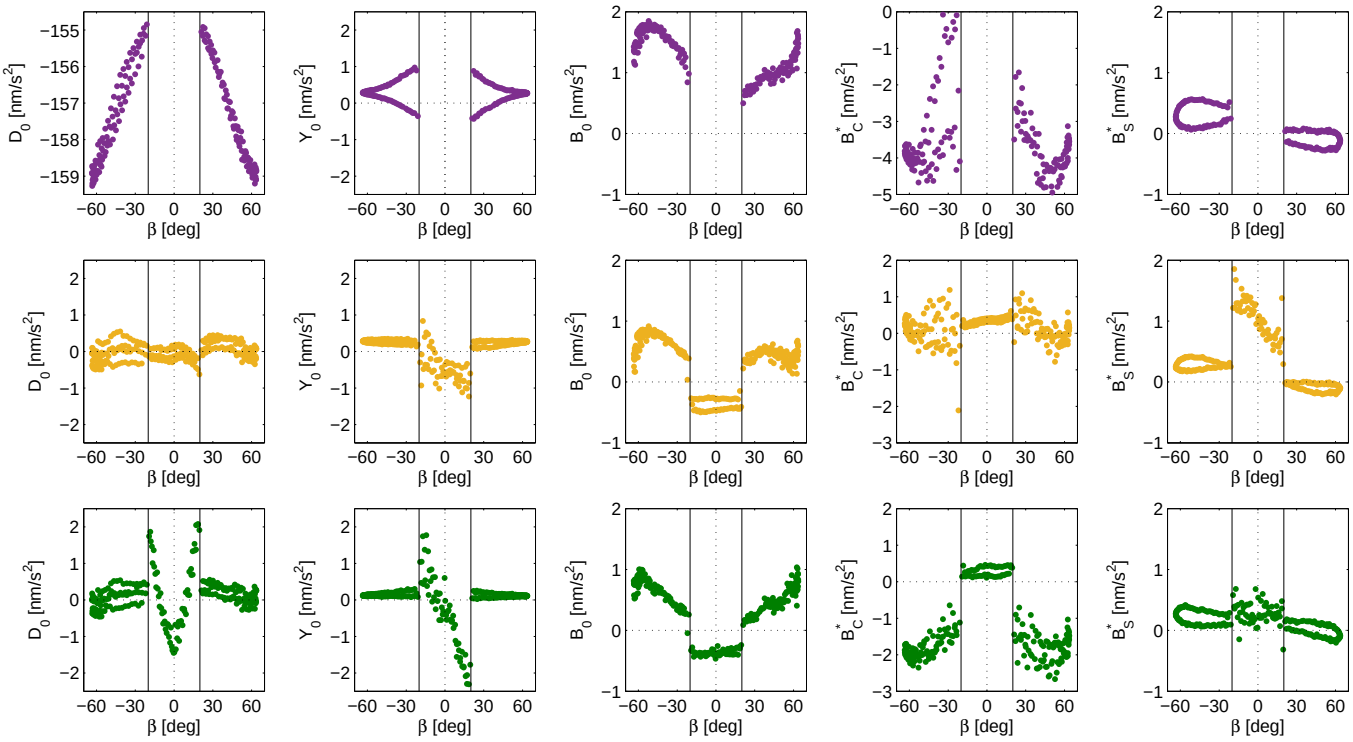

Figure 3: Estimated ECOM parameters: no a priori model (top), a priori box-wing model (middle), a priori ray-tracing model (bottom).

effects and a presumed mismatch of optical coefficients for the y-surfaces. For the box-wing model, these contributions were implicitly accounted for in the empirical tuning of the model coefficients resulting in significantly smaller ECOM parameters in ON mode.

The orbit prediction performance is a measure for the internal consistency of satellite orbits. More accurate orbit models provide more accurate orbit predictions, which are, e.g., important for real-time and near-real-time applications. Orbit predictions are thus a sensitive tool to assess the quality of different models, since model errors are accumulated by the orbit integration. In the present analysis, an orbit prediction covering three days is compared with a 3-day arc completely obtained from observations. Resulting median RMS values are listed in the left part of Table 3. The box-wing model is found to perform similar in YS and ON model. The ray-tracing model, in contrast, shows the smallest RMS values of less than $50\,\mathrm{cm}$ in YS mode, but a significantly increased RMS of almost $3\,\mathrm{m}$ in ON mode. The orbit prediction RMS of the ECOM-only models in YS model is clearly worse than that of the other test cases, thus illustrating the benefit of (semi-)analytical over empirical SRP models.

Another internal quality indicator are the day-boundary discontinuities (DBDs). They are computed as 3D difference of the orbit positions of two consecutive arcs at midnight. Median values for the DBDs are listed in the right part of Table 3. In YS mode, the box-wing model reduces the DBDs by a factor of more than two compared to the 5-parameter ECOM. Introducing the ray-tracing model results in DBDs of about two decimeters. The box-wing model has a similar performance in YS and ON mode, but the DBDs of the ray-tracing model are worse by a factor of two in ON mode compared to the YS mode due to the unmodeled thermal radiation effects. It may be noted that

Table 3: Median RMS values of 3-day orbit predictions w.r.t. orbit arcs based on observations and median day boundary discontinuities.

Solution	Pred. [cm]		DBD [cm]	
	YS	ON	YS	ON
5-par. ECOM	157	–	70	–
9-par. ECOM-2	99	–	15	–
Box-wing model	58	67	29	24
Ray-tracing	48	298	21	42

the lowest DBDs ($15\,\mathrm{cm}$) are obtained for the ECOM-2 model, which indicates a high goodness-of-fit when using an empirical model with a total of nine parameters. On the other hand, it is evident from the previously discussed prediction accuracy that the same model is unable to properly represent the real orbital dynamics over an extended data arc. Evidently, the combination of a proper a priori model with a modest amount of additional adjustment parameters provides the best compromise in terms of orbit representation and prediction performance.

The *accuracy* of the estimated satellite orbits can be evaluated by the independent (optic) satellite laser ranging (SLR) technique. Five SLR stations of the International Laser Ranging Service (ILRS; Pearlman et al., 2002) track QZS-1 on a regular basis: Beijing, Changchun, and Shanghai in China as well as Mount Stromlo and Yarragadee in Australia. For the analysis interval, a total of 2703 normal points are available, which includes 2040 normal points in YS mode and 663 in ON mode.

Table 4: Bias and standard deviation (STD) of QZS-1 SLR residuals.

Solution	YS mode		ON mode	
	Bias [cm]	STD [cm]	Bias [cm]	STD [cm]
5-par. ECOM	0.0	15.7	–	–
9-par. ECOM-2	−6.8	8.5	–	–
Box-wing model	2.6	7.8	6.2	8.7
Ray-tracing	−3.9	5.5	−1.9	14.2

Station coordinates are fixed to SLRF2014[2] and observations below 10° or exceeding an outlier limit of $1\,\mathrm{m}$ are excluded. Bias and standard deviation (STD) of the SLR residuals are listed in Table 4 for the four solutions and time series are plotted in Fig. 4. Whereas ECOM-2 shows a significant improvement compared to ECOM in terms of STD, it introduces a $-7\,\mathrm{cm}$ bias in YS mode. The STD of the box-wing model is similar to ECOM-2 and a factor of two smaller compared to ECOM in YS mode. The ray-tracing model shows the smallest SLR residuals of $5.5\,\mathrm{cm}$ STD in YS mode, which marks $30\,\%$ reduction compared to the box-wing model. However, the absolute value of the SLR bias increases also by about one third. The origin of this bias is unknown. Steigenberger et al. (2015b) showed that not modeling the shading caused by a plate extending beyond the core body of GIOVE-B introduces an SLR offset of almost $10\,\mathrm{cm}$. Small-scale structures of the satellite not covered by the current ray-tracing model might thus explain the $-4\,\mathrm{cm}$ bias in the SLR residuals of QZS-1 in YS mode. In ON mode, the STD of the box-wing model is slightly increased compared to YS mode. Like for the measures for precision, the ray-tracing model has an increased STD in ON mode due to unmodeled thermal radiation. However, the absolute value of the bias is reduced by a factor of two, whereas the bias of the box-wing model increases to $6\,\mathrm{cm}$ in ON mode.

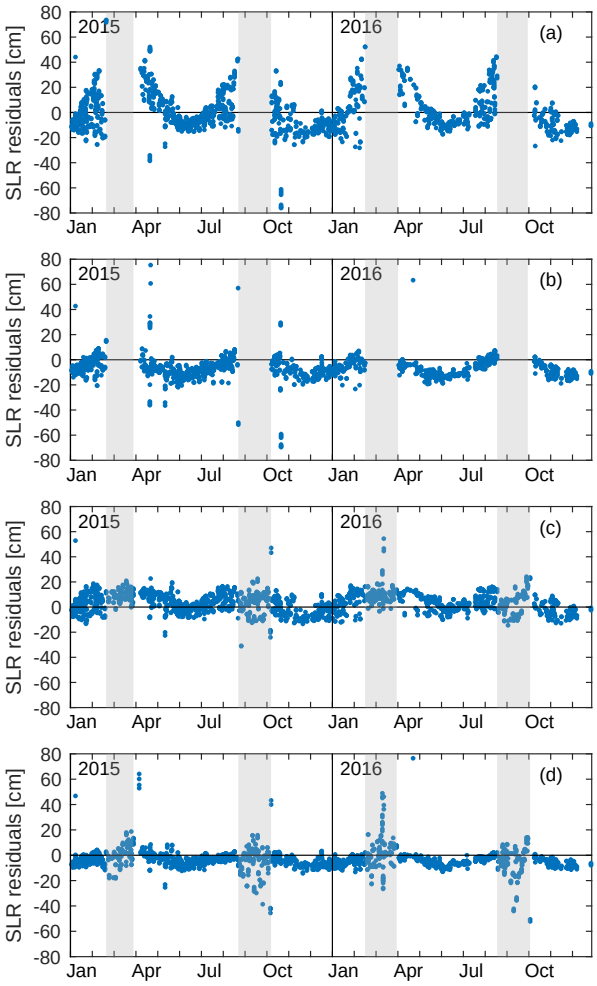

Figure 4: Satellite laser ranging residuals of QZS-1: (a) 5-parameter ECOM, (b) 9-parameter ECOM-2, (c) box-wing model, (d) ray-tracing model. The gray-shaded areas indicate the orbit-normal mode.

6 Summary and Conclusion

A CAD model of QZS-1 was developed based on a scaled paper model of the spacecraft. Using the OpticStudio software, a ray-tracing simulation of the interaction between the solar photons and the surface components of the QZS-1 satellite was computed. The ARPA software of the University of Padua was used to calculate the SRP acceleration from the OpticStudio output and assumed optical properties over a 1° grid of azimuth and elevation angles in the spacecraft frame.

The benefits of a ray-tracing model for the orbit determination quality was analyzed in terms of SLR residuals, day boundary discontinuities and RMS error of 3-day orbit predictions. With respect to the box-wing model, the ray-tracing model provides an improvement in YS mode of $8\,\mathrm{cm}$ in day boundary discontinuities, of $10\,\mathrm{cm}$ in the RMS of the 3-day orbit prediction errors and roughly a $2\,\mathrm{cm}$ improvement in the STD of the SLR residuals. However, the application of the ray-tracing model increased the bias of the SLR residuals to about $-4\,\mathrm{cm}$. The source of this bias is still unknown, but could be explained by small-scale structures of the satellite not covered by the current ray-tracing model and/or ignored by the relatively coarse grid resolution of $0.1\,\mathrm{m}\times0.1\,\mathrm{m}$.

In ON mode, the ray-tracing model performs worse than the adjusted box-wing model. This is, among others, due to thermal radiation that is implicitly considered in the empirically adjusted coefficients of the box-wing model, but neglected in the ray-tracing SRP-only model. The imbalance of thermal radiation from the optical surface reflectors on the $\pm y$-faces of the satellite contributes notable non-gravitational accelerations in ON mode but cannot be modeled analytically without knowledge of the satellite's thermal control system. Further improvements and, maybe, also the explanation of the $-4\,\mathrm{cm}$ SLR offset could be achieved with a more detailed ray-tracing model based on measured optical properties and a comprehensive CAD model of the satellite geometry. Moreover, with information about the thermal properties, a thermal radiation pressure analysis could be provided by the ARPA software. However, the publication of optical and thermal properties by the QZSS provider is still pending.

[2]available at ftp://cddis.nasa.gov/slr/products/resource

Acknowledgments

The Multi-GNSS Pilot Project (MGEX) of the International GNSS Service (IGS) and the International Laser Ranging Service (ILRS) are acknowledged for providing multi-GNSS and SLR observation data. We also thank the European Space Agency for granting access to the NAPEOS v3.3.1 software used in this study. Likewise, we would like to acknowledge the fast response and constructive comments of the three anonymous reviewers.

References

References

Adhya, S., 2005. Thermal re-radiation modelling for the precise prediction and determination of spacecraft orbits. Ph.D. thesis, University of London.

Agueda, A., Zandbergen, R., 2004. NAPEOS mathematical models and algorithms. Tech. Rep. NAPEOS-MM-01, iss. 3.0, 04/06/2004, ESA/ESOC, Darmstadt.

Arnold, D., Meindl, M., Beutler, G., Dach, R., Schaer, S., Lutz, S., Prange, L., Sosnica, K., Mervart, L., Jäggi, A., 2015. CODE's new solar radiation pressure model for GNSS orbit determination. J. Geod. 89 (8), 775–791, DOI 10.1007/s00190-015-0814-4.

Bar-Sever, Y. E., 1996. A new model for GPS yaw attitude. J. Geod. 70 (11), 714–723, DOI 10.1007/BF00867149.

Beutler, G., Brockmann, E., Gurtner, W., Hugentobler, U., Mervart, L., Rothacher, M., Verdun, A., 1994. Extended orbit modeling techniques at the CODE processing center of the International GPS Service for Geodynamics (IGS): Theory and initial results. Manuscr. Geod. 19 (6), 367–386.

Bock, Y., Melgar, D., 2016. Physical applications of GPS geodesy: a review. Rep. Prog. Phys. 79 (10), 106801, DOI 10.1088/0034-4885/79/10/106801.

Cabinet Office, 2017a. Quasi-Zenith Satellite System.
URL http://qzss.go.jp/en/index.html

Cabinet Office, 2017b. QZS-1 satellite information. Tech. Rep. SPI_QZS1, Government of Japan, National Space Policy Secretariat.
URL http://qzss.go.jp/en/technical/qzssinfo/index.html

Cabinet Office, 2018. The history information of QZS-1 operation. Tech. Rep. OHI-QZS1, Government of Japan, National Space Policy Secretariat.
URL http://qzss.go.jp/en/technical/qzssinfo/khp0mf0000000wuf-att/ohi-qzs1.pdf

Cerri, L., Berthias, J., Bertiger, W., Haines, B., Lemoine, F., Mercier, F., Ries, J., Willis, P., Zelensky, N., Ziebart, M., 2010. Precision orbit determination standards for the Jason series of altimeter missions. Marine Geod. 33, 379–418, DOI 10.1080/01490419.2010.488966.

Dow, J. M., Neilan, R. E., Rizos, C., 2009. The International GNSS Service in a changing landscape of Global Navigation Satellite Systems. J. Geod. 83 (3–4), 191–198, DOI 10.1007/s00190-008-0300-3.

Gini, F., 2014. GOCE precise non-gravitational force modeling for POD applications. Ph.D. thesis, Università degli Studi di Padova.

IGS, 2017. Daily 30-second observation data, NASA Crustal Dynamics Data Information System (CDDIS). DOI 10.5067/GNSS/gnss_daily_o_001.

Inaba, N., Matsumoto, A., Hase, H., Kogure, S., Sawabe, M., Terada, K., 2009. Design concept of Quasi Zenith Satellite System. Acta Astronaut. 65 (7), 1068–1075, DOI 10.1016/j.actaastro.2009.03.068.

Ishijima, Y., Inaba, N., Matsumoto, A., Terada, K., Yonechi, H., Ebisutani, H., Ukava, S., Okamoto, T., 2009. Design and developement of the first Quasi-Zenith Satellite attitude and orbit control system. In: 2009 IEEE Aerospace Conference. IEEE, pp. 1–8, DOI 10.1109/AERO.2009.4839537.

JAXA, 2010. Presskit first Quasi-Zenith Satellite System MICHIBIKI.
URL http://global.jaxa.jp/countdown/f18/pdf/presskit_michibiki_e.pdf

Knocke, P., 1989. Earth radiation pressure effects on satellites. Tech. Rep. CSR-98-1, Center for Space Research, University of Texas.

Kogure, S., 2016. Status update on the Quasi-Zenith Satellite System. In: ICG-11, Sochi, Russian Federation.

Kogure, S., Ganeshan, A. S., Montenbruck, O., 2017. Regional systems. In: Teunissen, P. G., Montenbruck, O. (Eds.), Springer Handbook of Global Navigation Satellite Systems. Springer, Ch. 11, pp. 305–337, DOI 10.1007/978-3-319-42928-1_11.

Li, Z., Ziebart, M., Bhattarai, S., Harrison, D., Grey, S., 2018. Fast solar radiation pressure modelling with ray tracing and multiple reflections. Adv. Space Res. 61 (9), 2352–2365, DOI 10.1016/j.asr.2018.02.019.

Melbourne, W. G., 1985. The case for ranging in GPS based geodetic systems. In: Goad, C. (Ed.), Proceedings of the First International Symposium on Precise Positioning with the Global Positioning System. U.S. Department of Commerce, Rockville, Maryland, pp. 373–386.

Milani, A., Nobili, A. M., Farinella, P., 1987. Non-gravitational Perturbations and Satellite Geodesy. Adam Hilger Ltd., Bristol, UK.

Montenbruck, O., Schmid, R., Mercier, F., Steigenberger, P., Noll, C., Fatkulin, R., Kogure, S., Ganeshan, A. S., 2015. GNSS satellite geometry and attitude models. Adv. Space Res. 56 (6), 1015–1029, DOI 10.1016/j.asr.2015.06.019.

Montenbruck, O., Steigenberger, P., Darugna, F., 2017a. Semi-analytical solar radiation pressure modeling for QZS-1 orbit-normal and yaw-steering attitude. Adv. Space Res. 59 (8), 2088–2100, DOI 10.1016/j.asr.2017.01.036.

Montenbruck, O., Steigenberger, P., Prange, L., Deng, Z., Zhao, Q., Perosanz, F., Romero, I., Noll, C., Stürze, A., Weber, G., Schmid, R., MacLeod, K., Schaer, S., 2017b. The Multi-GNSS Experiment (MGEX) of the International GNSS Service (IGS) – achievements, prospects and challenges. Adv. Space Res. 59 (7), 1671–1697, DOI 10.1016/j.asr.2017.01.011.

Pearlman, M., Degnan, J., Bosworth, J., 2002. The International Laser Ranging Service. Adv. Space Res. 30 (2), 125–143, DOI 10.1016/S0273-1177(02)00277-6.

Prange, L., Orliac, E., Dach, R., Arnold, D., Beutler, G., Schaer, S., Jäggi, A., 2017. CODE's five-system orbit and clock solution – the challenges of multi-GNSS data analyis. J. Geod.

91 (4), 345–360, DOI 10.1007/s00190-016-0968-8.

Rebischung, P., Altamimi, Z., Ray, J., Garayt, B., 2016a. The IGS contribution to ITRF2014. J. Geod. 90 (7), 611–630, DOI 10.1007/s00190-016-0897-6.

Rebischung, P., Schmid, R., Herring, T., 2016b. [IGSMAIL-7399] Upcoming switch to IGS14/igs14.atx. URL https://lists.igs.org/pipermail/igsmail/2016/001233.html

Rodriguez-Solano, C., Hugentobler, U., Steigenberger, P., 2012. Adjustable box-wing model for solar radiation pressure impacting GPS satellite. Adv. Space Res. 49 (7), 1113–1128, DOI 10.1016/j.asr.2012.01.016.

Rodriguez Solano, C. J., Nov. 2009. Impact of albedo modelling on GPS orbits. Master's thesis, TU München.

Springer, T., Beutler, G., Rothacher, M., 1999. A new solar radiation pressure model for GPS satellites. GPS Solut. 2 (3), 50–62, DOI 10.1007/PL00012757.

Steigenberger, P., Hugentobler, U., Loyer, S., Perosanz, F., Prange, L., Dach, R., Uhlemann, M., Gendt, G., Montenbruck, O., 2015a. Galileo orbit and clock quality of the IGS Multi-GNSS Experiment. Adv. Space Res. 55 (1), 269–281, DOI 10.1016/j.asr.2014.06.030.

Steigenberger, P., Montenbruck, O., Hugentobler, U., 2015b. GIOVE-B solar radiation pressure modeling for precise orbit determination. Adv. Space. Res. 55 (5), 1422–1431, DOI 10.1016/j.asr.2014.12.009.

Steigenberger, P., Thoelert, S., Montenbruck, O., 2018. GNSS satellite transmit power and its impact on orbit determination. J. Geod. 92 (6), 609–624, DOI 10.1007/s00190-017-1082-2.

Wübbena, G., 1985. Software developments for geodetic positioning with GPS using TI-4100 code and carrier measurements. In: Goad, C. (Ed.), Proceedings of the First International Symposium on Precise Positioning with the Global Positioning System. U.S. Department of Commerce, Rockville, Maryland, pp. 403–412.

Zhao, Q., Chen, G., Guo, J., Liu, J., Liu, X., 2018. An a priori solar radiation pressure model for the QZSS Michibiki satellite. J. Geod. 92 (2), 109–121, DOI 10.1007/s00190-017-1048-4.

Ziebart, M., 2004. Generalized analytical solar radiation pressure modeling algorithm for spacecraft of complex shape. J. Spacecr. Rockets 41 (5), 840–848, DOI 10.2514/1.13097.